

# Igneous dikes on Mars revealed by Mars Orbiter Laser Altimeter topography

Richard A. Schultz  
Chris H. Okubo  
Cheryl L. Goudy  
Scott J. Wilkins\*

Geomechanics–Rock Fracture Group, Department of Geological Sciences, University of Nevada, Reno, Nevada 89557, USA

## ABSTRACT

The origin of Martian grabens has remained controversial for decades, given the non-uniqueness of graben morphology and conflicting interpretations of dike-induced or faulting-based formation processes. We use measurements from the Mars Orbiter Laser Altimeter to identify the characteristic topographic signature at the surface of an igneous dike beneath a Martian graben. Our results suggest that this subtle but diagnostic signature can be used to test competing interpretations of the formation of grabens and associated fissures and collapse depressions.

**Keywords:** Mars, dikes, Tharsis, tectonics, MOLA.

## INTRODUCTION

Martian grabens in the Tharsis region of Mars have been interpreted, or assumed, to form as a result of either faulting-based processes (i.e., near-surface crustal extension; see Banerdt et al., 1992; Phillips et al., 2001) or volcanic processes (i.e., intrusion and dilation of mafic igneous dikes in the near-surface region; see Mège and Masson, 1996; Wilson and Head, 2002; Ernst et al., 2001; Mège et al., 2003, for reviews and discussion). A definitive interpretation has remained elusive, however, because the structure and morphology of grabens alone cannot be used to distinguish between them. Results from detailed study of terrestrial grabens demonstrate that a characteristic topographic signature at the surface develops above a near-surface igneous dike (e.g., Pollard et al., 1983; Mastin and Pollard, 1988) on which the fault-related topography of the associated graben is superimposed (e.g., Rubin and Pollard, 1988; Rubin, 1992). The presence of dike-related topography is necessary and sufficient to infer the presence of a dilated igneous dike at shallow depth beneath the graben.

In this paper we report the discovery of the characteristic topographic signature at the Martian surface of an igneous dike at shallow depth, which is associated with part of a Tharsis radial graben (Fig. 1). We then use standard methods to model the topography and thereby infer the depth, driving pressure, and dilation of the subsurface dike.

## METHODS

Topographic measurements from the Mars Orbiter Laser Altimeter (MOLA) Precision Experiment Data Record (PEDR) data set (Smith et al., 2003) are used to characterize the cross-strike topography of the Tharsis radial graben. These data are a series of spot elevations taken along the ground track of the Mars Global Surveyor (MGS) satellite. Spot elevations are spaced ~300 m center-to-center along the MGS ground track, and the footprint for each spot elevation measurement is ~168 m in diameter (Smith et al., 2003). Each measurement has a vertical precision of typically <1 m (Neumann et al., 2001). Four closely spaced PEDR tracks are selected across a typical Tharsis radial graben within the Memnonia region of Mars (Fig. 1). Track-to-track separation distances range between 1.8 and 2.4 km, and these tracks are subperpendicular to the trend of the graben. The effect of a slight north-dipping regional slope is removed from

each transect by trigonometric reduction of subsequent along-track elevation values using a gradient of <0.1°.

Within the four MOLA transects, an ~4-km-wide, 10–15-m-deep graben is consistently revealed; the north rim of the graben is ~5 m higher than the south rim (Fig. 2). Visual comparison of these tracks shows that in general, the flanks of the graben have an overall concave-down morphology, superimposed with meter-scale topographic variations. The topographic highs of the graben flanks are several kilometers from the rim of the graben.

Careful analysis of data collected by the Mars Orbiter Camera (e.g., M0804125, M0002948) reveals rough surficial material that extends for tens of kilometers from in situ layered rock mass exposures within the upper graben walls. The lower slopes of the graben walls are covered by talus fans; dunes with tens of meters wavelength occur in patches along the graben floors and flanks. Evidence

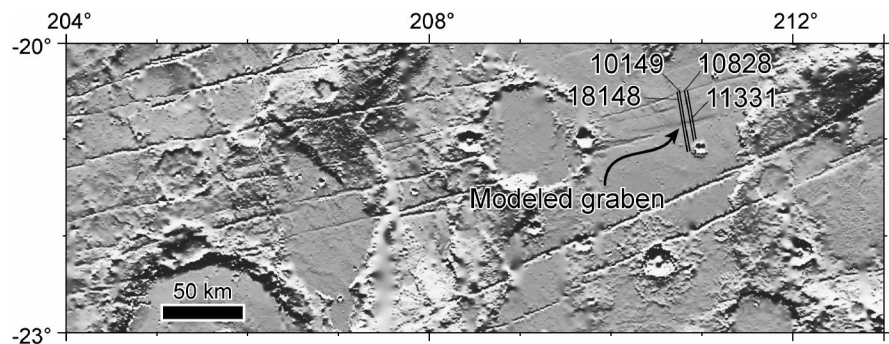


**Figure 1. Shaded relief map of northeast-trending Tharsis-radial grabens within Memnonia region of Mars. Shown are locations and numbers of Mars Orbiter Laser Altimeter tracks used for graben modeled in this study.**

\*Present address: Shell International Exploration and Production, Inc., Bellaire Technology Center, P.O. Box 481, Houston, Texas 77001, USA.

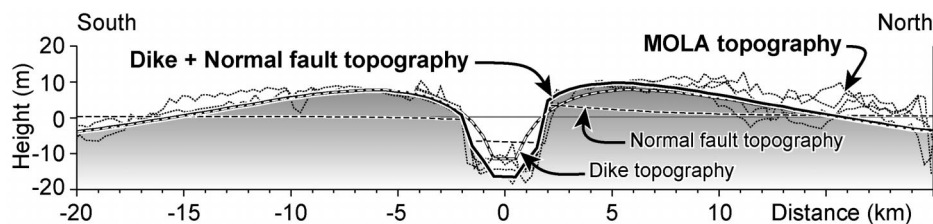


**Figure 2.** Mars Orbiter Laser Altimeter (MOLA) Precision Experiment Data Record topographic profiles of modeled graben (dashed lines), and best-fit model surface displacements (solid lines).

of fluvial erosion (e.g., gullies or channels) is not observed. Further, thermal emission imaging system data (e.g., I07664008, I06940005) reveal areas of high thermal inertia along the talus fans at the base of the graben walls, with areas of lowest thermal inertia corresponding to the rock mass exposures and slightly higher thermal inertia within the graben floors and surrounding plains. These observations are consistent with minimal fluvial erosion and eolian sedimentation; the bulk of the sediment is derived locally from the graben walls (colluvium). Therefore, with the exception of the talus-covered lower graben walls, the MOLA data provide a reliable measure of graben-related topography.

In order to model the MOLA topography of Figure 2, we use the two-dimensional boundary element program FAULT (Schultz and Aydin, 1990; Schultz, 1992; Bruhn and Schultz, 1996; Schultz and Balasko, 2003; Okubo and Schultz, 2004), which utilizes the displacement discontinuity method (Crouch, 1976; Crouch and Starfield, 1983). In these models, we prescribe a crustal elastic (Young's) modulus of 60 GPa and a Poisson's ratio of 0.25, with rock friction angle of 30° and 0.5 MPa fault cohesion (values appropriate to the rock mass adjoining a dike wall). Crustal density is taken to be 2600 kg/m<sup>3</sup> and magma density is 2200 kg/m<sup>3</sup>. Far-field (regional) stresses are defined as gradients that increase with depth, with the maximum compressive remote stress ( $\sigma_1 = \sigma_v$ ) prescribed as a lithostatic load gradient for Martian gravity ( $g = 3.71 \text{ m/s}^2$ ) and the least horizontal (compressive) stress  $\sigma_3 = \sigma_h$  defined as a positive fraction (e.g., 1/2) of  $\sigma_v$ , following measurements of terrestrial crustal stress states (e.g., McGarr and Gay, 1978; Plumb, 1994). Dike opening is driven by hydrostatic magma pressure with zero hydrostatic head. The model calculates the distribution and magnitude of displacements along each model dike and fault segment, along with the attendant crustal displacements. Natural variations in these model parameters would change our results in detail but would not alter our conclusions. This approach was previously used to successfully model the surface topography of Martian nor-

mal faults (Schultz and Lin, 2001; Wilkins and Schultz, 2003) and thrust faults (Schultz and Watters, 2001).

Work by Rubin and Pollard (1988) and Rubin (1992) shows that dike-induced graben formation occurs in two distinct stages. First, synthetic normal faults nucleate onto newly formed joints in the dike's near-tip region and slip on either side and ahead of the oncoming propagating dike tip. Then, as the dike tip propagates past these faults, dike-induced dilation increases the magnitude of the local horizontal compressive stress, which acts to prevent further frictional slip on the graben-bounding faults. In this way, crustal displacements around dike-induced graben are the sum of normal fault-related and dike-related displacements. Further, Rubin and Pollard (1988) showed that observed dike-induced graben displacements in Iceland are best fit with dike- and normal fault-induced displacements, instead of dike-induced displacements alone. Accordingly, our model graben displacements are determined by summing normal fault-induced displacement vectors with dike-induced displacement vectors. In order to match the MOLA-observed graben topography, the dike and fault geometry, as well as far-field driving stresses, are iteratively varied until the resulting model graben topography fits MOLA observations.

The topography measured by MOLA across a Martian graben is the cumulative change resulting from the total growth of any dikes and faults associated with the graben. In contrast, Rubin and Pollard (1988) and others used the change in surface topography before and after a single intrusion event to calculate the dike parameters for that event alone. By fitting the MOLA topography with the calculated topography due to a dike, we obtain the total dilation regardless of whether it was achieved in a single or multiple episode of magma inflation.

## RESULTS AND DISCUSSION

The best-fit model surface displacements are shown in Figure 2 and the corresponding normal fault and dike geometry is shown in Figure 3. Two synthetic normal faults dip

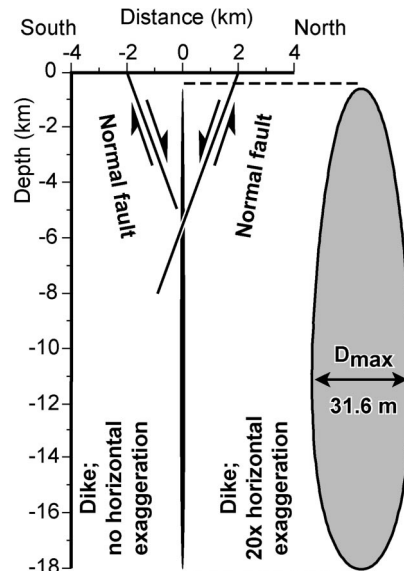


**Figure 3.** Model normal fault and dike geometry corresponding to best-fit surface displacements in Figure 2.

ward the dike at 70°, and the surface-breaking upper tips of both faults are located 2 km from the center of the graben. Downdip fault heights are 5.3 km for the north-dipping fault and 8.5 km for the south-dipping fault. These faults do not crosscut each other, but the south-dipping fault intersects the location of the superposed dike. The upper tip of the dike is at 0.5 km depth and centered below the graben. The dike is vertical and 17.5 km tall. Model-predicted dike opening displacements show a skewed elliptical displacement distribution, with 31.6 m of maximum dike opening,  $D_{max}$ , at 10.9 km depth. The predicted cross-sectional area of the dike is 0.449 km<sup>2</sup>. The best-fit ratio of far-field stress gradients is  $\sigma_h = 0.4\sigma_v$ ; this ratio is insufficient for normal faulting due to remote stress alone, requiring the additional contribution of the dike's near-tip stress field to promote normal faulting and graben formation. Using this model geometry, the MOLA-observed graben topography is fit by three complete cycles of normal faulting and dike intrusion, rather than one single high-strain event. Thus, the cumulative geologic dike opening predicted for this graben is 94.8 m. This model geometry for multiple graben-forming events produces a good fit to the graben flanks, as well as interior of the graben.

Alternatively, the topography of this graben (outside the faults) can also be fit by a single cycle of normal faulting and dike intrusion. This single-event model geometry produces a good fit to the graben flanks, but underpredicts the depth of the graben by ~10 m. Here, the dike and normal fault geometry of Figure 3 is adjusted to produce higher strains. In this single-event scenario, two synthetic normal faults dip

80°, and the upper fault tips are surface breaking and located 2 km from the center of the graben. Downdip fault heights are 11.0 km for the north-dipping fault and 17.0 km for the south-dipping fault. These faults do not cross-cut each other, but both intersect the location of the superposed dike. The upper tip of the dike is at 0.1 km depth and centered below the graben. The dike dips 88° to the south and is 25.9 km tall. Model-predicted dike opening displacements show a skewed elliptical displacement distribution, with a  $D_{\max}$  of 71.6 m at 14.6 km depth. The predicted cross-sectional area of the dike is 1.574 km<sup>2</sup>, and the best-fit ratio of far-field stress gradients remains at  $\sigma_h = 0.4\sigma_v$ . An acceptable fit to the topography, both within and beyond the graben, is only achieved for the multiple-event case in which larger displacements occur on smaller structures (dikes and graben-bounding faults). Dike depths of 20–30 km imply magma transport well within the Martian crust (e.g., Zuber, 2001).

Our model-predicted normal-fault surface displacements outline a typical faulting-based graben; the flanks of the faulting-based graben are concave up and topographic flank highs are located at the graben rim. Conversely, predicted surface displacements above the dike alone show uplifted flanks with concave-down slopes. The topographic highs of the dike-induced flanks are located ~6 km distant on either side of the surface projection of the dike—well beyond the graben rim. Summing the predicted dike- and normal fault-induced surface displacements yields a best-fit model graben characterized by concave-down flanks with topographic flanking highs located several kilometers from the graben rim, consistent with MOLA observations. Further, the magnitude of best-fit model relief, measured from graben floor to rim, is also consistent with MOLA. Conversely, faulting-based displacements alone predict graben flanks with concave-up slopes and flank topographic highs at the graben rim (e.g., Stein et al., 1988; Cohen, 1999).

The topography within the graben is fit only approximately by the models. As discussed by Rubin (1992), increased fracture densities around the dike leading to locally reduced modulus beneath the graben, as documented beneath Icelandic volcanic grabens, could promote greater subsidence of the graben floor than the values predicted by an elastic model. Other factors, such as local anisotropy, mass increase due to the dike (both beneath the graben floor), dike tip cavities (Rubin, 1993), and explicit consideration of the timing of fault slip and dike dilation (Rubin, 1992), stopping into the dike cavity (Okubo and Martel, 1998), and sedimentation within the graben (e.g.,

Grosfils et al., 2003) may also improve the fit within the Martian graben. Beyond the graben faults, however, the model provides a reliable means for assessing the presence of a dike beneath a graben.

These results show that the topography of the modeled Tharsis radial graben is most consistent with a dike-induced origin, and least consistent with a faulting-based origin. Therefore, these results strongly support previous interpretations that at least some Tharsis radial grabens formed in response to dike propagation. Further, our approach and results provide a straightforward criterion for evaluating the origin (faulting based vs. dike induced) of grabens on planetary surfaces based on topography. Flanks of dike-induced grabens are predicted to have concave-down slopes. Conversely, flanks of faulting-based grabens are predicted to have concave-up slopes.

## CONCLUSIONS AND IMPLICATIONS

We demonstrate that the topography across a 10-km-long Tharsis radial graben segment within the Memnonia Fossae array is consistent with a subjacent dike that extends to ~18 km depth with a maximum total dilation of ~95 m. The amplitude of surface uplift associated with this dike, 15–20 m, is subtle yet recognizable in MOLA profiles. Suggestions of substantially larger dikes (e.g., to depths of ~100 km; Wilson and Head, 2002) should be testable from similar analyses of MOLA data. Our results indicate that at least one graben segment in Tharsis (i.e., Fig. 1) overlies a dike, supporting previous suggestions of near-surface magma transport for that area. However, our preliminary assessment of other Tharsis radial grabens does not consistently reveal dike-related topographic signatures, and thus we infer that Tharsis grabens may not reflect faulting-based or dike-induced origins along their entire extent. Other classes of Martian structures such as fissures and collapse depressions (including those with apparent fluid breakouts) that have been interpreted as the surface expression of shallow dikes (e.g., Burr et al., 2002; Russell and Head, 2003) may also reveal the presence (or absence) of dikes through analysis of their topography.

## ACKNOWLEDGMENTS

This test of Martian dikes was originally conceived on publication of Rubín and Pollard's (1988) classic paper and is now possible with the availability of Mars Orbiter Laser Altimeter topography of sufficiently fine resolution. Reviews by Daniel Mège and an anonymous referee sharpened the final paper. We thank Lionel Wilson for cordial and informative discussions on Martian dike models. This work was supported by National Aeronautics and Space Administration's Planetary Geology and Geophysics Program and the Mars Data Analysis Program.

## REFERENCES CITED

- Banerdt, W.B., Golombek, M.P., and Tanaka, K.L., 1992, Stress and tectonics on Mars, *in* Kieffer, H.H., et al., eds., *Mars: Tucson*, University of Arizona Press, p. 249–297.
- Bruhn, R.L., and Schultz, R.A., 1996, Geometry and slip distribution in normal fault systems—Implications for mechanics and fault-related hazards: *Journal of Geophysical Research*, v. 101, p. 3401–3412.
- Burr, D.M., McEwen, A.S., and Sakimoto, S.E.H., 2002, Recent aqueous floods from the Cerberus Fossae, Mars: *Geophysical Research Letters*, v. 29, 1013, doi: 10.1029/2001GL013345.
- Cohen, S.C., 1999, Numerical models of crustal deformation in seismic zones: *Advances in Geophysics*, v. 41, p. 133–231.
- Crouch, S.L., 1976, Solution of plane elasticity problems by the displacement discontinuity method: *International Journal of Numerical Methods in Engineering*, v. 10, p. 301–343.
- Crouch, S.L., and Starfield, A.M., 1983, *Boundary element methods in solid mechanics*: London, George Allen & Unwin, 322 p.
- Ernst, R.E., Grosfils, E.B., and Mège, D., 2001, Giant mafic dyke swarms on Earth, Venus and Mars: *Annual Reviews of Earth and Planetary Science*, v. 29, p. 489–534.
- Grosfils, E.B., Schultz, R.A., and Kroeger, G., 2003, Geophysical exploration within northern Devils Lane graben, Canyonlands National Park, Utah—Implications for sediment thickness and tectonic evolution: *Journal of Structural Geology*, v. 25, p. 455–467.
- Mastin, L.G., and Pollard, D.D., 1988, Surface deformation and shallow dike intrusion processes at Inyo Craters, Long Valley, California: *Journal of Geophysical Research*, v. 93, p. 13,221–13,235.
- McGarr, A., and Gay, N.C., 1978, State of stress in the Earth's crust: *Annual Reviews of Earth and Planetary Science*, v. 6, p. 405–436.
- Mège, D., and Masson, P., 1996, A plume tectonics model for the Tharsis province, Mars: *Planetary and Space Science*, v. 44, p. 1499–1546.
- Mège, D., Cook, A.C., Garel, E., Lagabrielle, Y., and Cormier, M.-H., 2003, Volcanic rifting at Martian graben: *Journal of Geophysical Research*, v. 108, 5044, doi: 10.1029/2002JE001852.
- Neumann, G.A., Rowlands, D.D., Lemoine, F.G., Smith, D.E., and Zuber, M.T., 2001, Crossover analysis of Mars Orbiter Laser Altimeter data: *Journal of Geophysical Research*, v. 106, p. 23,753–23,768.
- Okubo, C.H., and Martel, S.J., 1998, Pit crater formation on Kilauea volcano, Hawaii: *Journal of Volcanology and Geothermal Research*, v. 86, p. 1–18.
- Okubo, C.H., and Schultz, R.A., 2004, Mechanical stratigraphy in the western equatorial region of Mars based on thrust fault-related fold topography and implications for near-surface volatile reservoirs: *Geological Society of America Bulletin*, v. 116, p. 594–605.
- Phillips, R.J., Zuber, M.T., Solomon, S.C., Golombek, M.P., Jakosky, B.M., Banerdt, W.B., Smith, D.E., Williams, R.M.E., Hynes, B.M., Aharonson, O., and Hauck, S.A., II, 2001, Ancient geodynamics and global-scale hydrology on Mars: *Science*, v. 291, p. 2587–2591.
- Plumb, R.A., 1994, Variations of the least horizontal stress magnitude in sedimentary rocks, *in* Nelson, P.P., and Laubach, S.E., eds., *Rock mechanics—Models and measurements, challenges from industry*: Rotterdam, Balkema, 1144 p.

Pollard, D.D., Delaney, P.T., Duffield, W.A., Endo, E.T., and Okamura, A.T., 1983, Surface deformation in volcanic rift zones: *Tectonophysics*, v. 94, p. 541–584.

Rubin, A.M., 1992, Dike-induced faulting and graben subsidence in volcanic rift zones: *Journal of Geophysical Research*, v. 97, p. 1839–1858.

Rubin, A.M., 1993, Tensile fracture of rock at high confining pressure—Implications for dike propagation: *Journal of Geophysical Research*, v. 98, p. 15,919–15,935.

Rubin, A.M., and Pollard, D.D., 1988, Dike-induced faulting in rift zones of Iceland and Afar: *Geology*, v. 16, p. 413–417.

Russell, P.S., and Head, J.W., 2003, Elysium-Utopia flows as mega-lahars—A model of dike intrusion, cryosphere cracking, and water-sediment release: *Journal of Geophysical Research*, v. 108, 5064, doi: 10.1029/2002JE001995.

Schultz, R.A., 1992, Mechanics of curved slip surfaces in rock: *Engineering Analysis with Boundary Elements*, v. 10, p. 147–154.

Schultz, R.A., and Aydin, A., 1990, Formation of

interior basins associated with curved faults in Alaska: *Tectonics*, v. 9, p. 1387–1407.

Schultz, R.A., and Balasko, C.M., 2003, Growth of deformation bands into echelon and ladder geometries: *Geophysical Research Letters*, v. 30, 2033, doi: 10.1029/2003GL018449.

Schultz, R.A., and Lin, J., 2001, Three-dimensional normal faulting models of Valles Marineris, Mars, and geodynamic implications: *Journal of Geophysical Research*, v. 106, p. 16,549–16,566.

Schultz, R.A., and Watters, T.R., 2001, Forward mechanical modeling of the Amenthes Rupes thrust fault on Mars: *Geophysical Research Letters*, v. 28, p. 4659–4662.

Smith, D.E., Neumann, G.A., Ford, P.G., Arvidson, R.E., Guinness, E.A., and Slavney, S., 2003, Mars Global Surveyor Laser Altimeter Precision Experiment Data Record, MGS-MOLA-3-PEDR-L1A-V1. 0, NASA Planetary Data System.

Stein, R.S., King, G.C.P., and Rundle, J.B., 1988, The growth of geological structures by repeated earthquakes 2. Field examples of con-

tinental dip-slip faults: *Journal of Geophysical Research*, v. 93, p. 13,319–13,331.

Wilkins, S.J., and Schultz, R.A., 2003, Cross faults in extensional settings—Stress triggering, displacement localization, and implications for the origin of blunt troughs in Valles Marineris, Mars: *Journal of Geophysical Research*, v. 108, 5056, doi: 10.1029/2002JE001968.

Wilson, L., and Head, J.W., 2002, Tharsis-radial graben system as the surface manifestation of plume-related dike intrusion complexes—Models and implications: *Journal of Geophysical Research*, v. 107, 5057, doi: 10.1029/2001JE001593.

Zuber, M.T., 2001, The crust and mantle of Mars: *Nature*, v. 412, p. 220–227.

Manuscript received 12 February 2004  
 Revised manuscript received 20 May 2004  
 Manuscript accepted 21 May 2004

Printed in USA

## CORRECTION

### Zirconolite: A new U-Pb chronometer for mafic igneous rocks: Correction

Birger Rasmussen and Ian R. Fletcher

*Geology*, v. 32, p. 785–788 (September 2004)

An error occurred in all three figures: the  $\pm$  signs appeared as  $-$  signs. The corrected versions (with  $\pm$  signs intact) appear here.

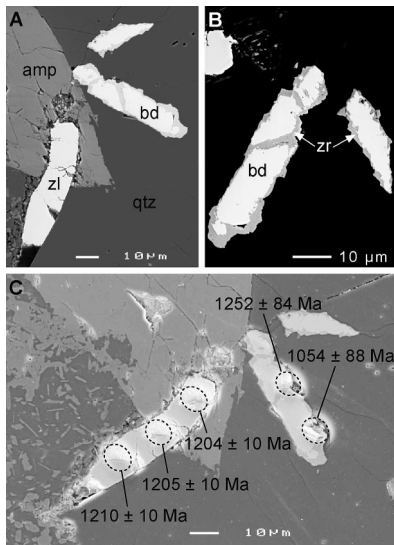


**Figure 1. A:** Backscattered electron microscope (BSEM) image of elongate zirconolite crystal (zl) partly enclosed in amphibole (amp), altered plagioclase (bottom left) and quartz (qtz), and two baddeleyite crystals (bd) in quartz. **B:** BSEM image of baddeleyite crystals showing thin alteration rims composed of polycrystalline zircon (zr). **C:** Secondary electron image of A showing location of SHRIMP analytical pits and corresponding  $^{207}\text{Pb}/^{206}\text{Pb}$  dates given at  $1\sigma$ . Low precision of two baddeleyite analyses is partly due to overlap of primary ion beam onto adjacent quartz.

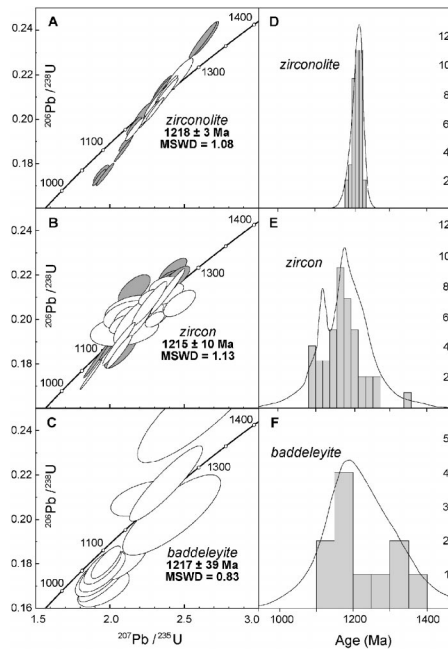


**Figure 2. Concordia plots showing Stirling dolerite SHRIMP U-Pb data for (A) zirconolite, (B) zircon, and (C) baddeleyite, and probability density plots illustrating distribution of  $^{207}\text{Pb}/^{206}\text{Pb}$  dates for (D) zirconolite, (E) zircon, and (F) baddeleyite. In A and B, first analyses on each grain are shown unshaded; subsequent analyses are shaded. Data not used in age determinations are not plotted. For zirconolite, U/Pb normalization procedure and method of assigning precision plotted for Pb/U are described in Appendix DR1 (see text footnote 1).**

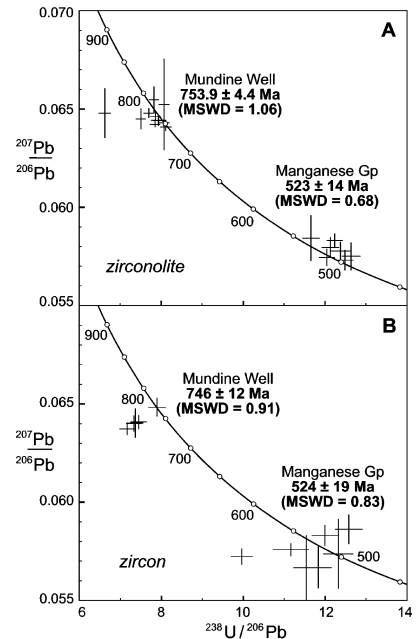


**Figure 3. Concordia plots of U-Pb data for (A) zirconolite, and (B) zircon from Mundine Well dike sample and Manganese Group sill. Zirconolite U-Pb data are normalized to reference 1215 Ma age for Stirling zirconolite. Most discordant Mundine Well analysis was not used in age calculation. For zirconolite, U/Pb normalization procedure and method of assigning precision plotted for Pb/U are described in Appendix DR1 (see text footnote 1).**